Atmos. Chem. Phys., 25, 2829–2844, 2025
https://doi.org/10.5194/acp-25-2829-2025

Atmospheric Chemistry and Physics
Open Access
EGU

Research article

A novel formation mechanism of sulfamic acid and its enhancing effect on methanesulfonic acid–methylamine aerosol particle formation in agriculture-developed and coastal industrial areas

Hui Wang[1,★], Shuqin Wei[1,★], Jihuan Yang[1], Yanlong Yang[1], Rongrong Li[1], Rui Wang[1], Chongqin Zhu[2], Tianlei Zhang[1], and Changming Zhang[3]

[1]Shaanxi Key Laboratory of Catalysis, School of Chemical & Environment Science, Shaanxi University of Technology, Hanzhong, Shaanxi 723001, P. R. China
[2]College of Chemistry, Key Laboratory of Theoretical & Computational Photochemistry of Ministry of Education, Beijing Normal University, Beijing 100190, China
[3]School of Mechanical Engineering, Shaanxi University of Technology, Hanzhong, Shaanxi 723001, P. R. China
★These authors contributed equally to this work.

Correspondence: Chongqin Zhu (cqzhu@bnu.edu.cn) and Tianlei Zhang (ztianlei88@163.com)

Received: 22 August 2024 – Discussion started: 22 October 2024
Revised: 28 December 2024 – Accepted: 17 January 2025 – Published: 7 March 2025

Abstract. Sulfamic acid (SFA) significantly impacts atmospheric pollution and poses potential risks to human health. Although traditional sources of SFA and their role in sulfuric acid–dimethylamine new particle formation (NPF) have received increasing attention, the formation mechanism of SFA from $HNSO_2$ hydrolysis with methanesulfonic acid (MSA) and its enhancing effect on MSA-methylamine (MA) NPF have not been studied, which will limit understanding on the source and loss of SFA in agriculture-developed and coastal industrial areas. Here, the gaseous and interfacial formation of SFA from $HNSO_2$ hydrolysis with MSA was investigated using quantum chemical calculations and Born–Oppenheimer molecular dynamics (BOMD) simulations. Furthermore, the role of SFA in the MSA-MA system was assessed using the Atmospheric Cluster Dynamic Code (ACDC) kinetic model. Our simulation results indicate that the gaseous SFA formation from the hydrolysis of $HNSO_2$ with MSA can be competitive with that catalyzed by H_2O within an altitude of 5–15 km. At the air–water interface, two types of reactions, the ion-forming mechanism and the proton exchange mechanism to form the $SFA^- \ldots H_3O^+$ ion pair, were observed on the timescale of picoseconds. Considering the overall environment of sulfuric acid emission reduction, the present findings suggest that SFA may play a significant role in NPF and the growth of aerosol particles, as (i) SFA can directly participate in the formation of MSA-MA-based clusters and enhance the rate of NPF from these clusters by approximately 10^3 times at 278.15 K and (ii) the SFA^- species at the air–water interface can attract gaseous molecules to the aqueous surface and thus promote particle growth.

Published by Copernicus Publications on behalf of the European Geosciences Union.

1 Introduction

As a well-studied nitrogen derivative of sulfuric acid (Rennebaum et al., 2024), sulfamic acid (SFA) was not only recognized as a potent aerosol and cloud-nucleating agent (Xue et al., 2024; Zhang et al., 2023b; Pszona et al., 2015; Li et al., 2018) but can also harm human health through atmospheric deposition into water bodies (Van Stempvoort et al., 2019). In agriculture-developed and industrial areas with high ammonia (NH_3) concentrations, such as the Yangtze River Delta in China (Yu et al., 2020), the Indo-Gangetic Plains (Kuttippurath et al., 2020), Pakistan, Bangladesh (Warner et al., 2016), and southern Italy (Tang et al., 2021), the atmospheric concentration of SFA estimated by the theoretical method of CCSD(T)-F12/cc-pVDZ-F12//M06-2X/6-311++G(3df,3pd) (Li et al., 2018) was expected to reach up to 10^8 molec. cm^{-3}, thus leading to it becoming a significant air pollutant; therefore, the sources of SFA in the atmosphere have been focused by several groups (Lovejoy and Hanson, 1996; Pszona et al., 2015; Li et al., 2018; Larson and Tao, 2001; Manonmani et al., 2020; Zhang et al., 2022b). The traditional source of SFA was mainly taken from the ammonolysis of SO_3 (Lovejoy and Hanson, 1996; Larson and Tao, 2001; Li et al., 2018). Experimentally, the rate coefficient for the ammonolysis of SO_3 was detected to be 2.0×10^{-11} cm^3 $molec.^{-1}$ s^{-1} at 295 K (Lovejoy and Hanson, 1996), which was close to the value for the hydrolysis of SO_3 assisted by water molecules (10^{-11}–10^{-10} cm^3 $molec.^{-1}$ s^{-1}) (Kim et al., 1998; Hirota et al., 1996; Shi et al., 1994; Kolb et al., 1994; Long et al., 2013, 2023; Ding et al., 2023; Cheng et al., 2023; Wang et al., 2024). Theoretically, the ammonolysis of SO_3 to produce SFA can be catalyzed by NH_3. In arid and heavily polluted regions with high NH_3 concentrations, the effective rate coefficient for the ammonolysis of SO_3 can be sufficiently rapid, making it competitive with the conventional loss pathway of SO_3 with water (Li et al., 2018).

In addition to the ammonolysis of SO_3, new sources of SFA formation have received increasing attention (Zhang et al., 2022b; Manonmani et al., 2020; Li et al., 2018; Xue et al., 2024). The existence of $HNSO_2$ was proposed in the reaction between SO_3 and NH_3 and was regarded as the most stable for nine different isomers of $HNSO_2$, HONSO, HOSNO, HOS(O)N, $HSNO_2$, HSONO, HON(O)S, HOOSN, and HOONS (Deng et al., 2016). Owing to its similarity to SO_3 and the potential role of SO_3 in the atmosphere, the hydrolysis of $HNSO_2$ to produce SFA formation has been the focus of several groups (Zhang et al., 2022b; Manonmani et al., 2020). As the direct hydrolysis of $HNSO_2$ with a high-energy barrier hardly takes place in the gas phase (Zhang et al., 2022b; Manonmani et al., 2020), the addition of a second water molecule (Manonmani et al., 2020), formic acid (H_2SO_4), and sulfuric acid (SA) (Zhang et al., 2022b) has been proven to promote the product of SFA through the hydrolysis of $HNSO_2$. It was noted that, with the global reduction in the concentration of H_2SO_4 resulting from SO_2 emission restrictions, the contribution of methanesulfonic acid (MSA) to aerosol nucleation has received the widespread attention of scientists. As a major inorganic acidic air pollutant (Chen et al., 2020), the concentration of MSA in the atmosphere was noted to be notably high across various regions, spanning from coastal to continental, with levels found to be between 10% and 250 % of those measured for SA (Shen et al., 2019, 2020; Dawson et al., 2012; Bork et al., 2014a; Berresheim et al., 2002; Hu et al., 2023). However, to the best of our knowledge, the gaseous hydrolysis of $HNSO_2$ with MSA has not yet been investigated, which will confine the understanding of the source of SFA to regions with significant pollution and high levels of MSA. Thus, understanding the hydrolysis of $HNSO_2$ with MSA in the gas phase was necessary for exploring its impact on aerosols and human health.

$$HNSO_2 + H_2O + MSA \rightarrow SFA + MSA \quad (1)$$

As a supplement to gas-phase reactions, interfacial reactions at the air–water interface can not only accelerate the rates of atmospheric reactions but may also introduce new mechanisms (Freeling et al., 2020; Zhong et al., 2019). For instance, the Criegee intermediates reacting with MSA at the air–water interface can form the ion pair of $CH_3C(H)(OOH)(SO_3CH_3)$ anhydride and H_3O^+ (Ma et al., 2020), which differs from the corresponding gaseous reaction where the MSA molecule acts solely as a reactant reacting with Criegee intermediates directly. As far as we know, $HNSO_2$ exhibits a significant interfacial preference, due to the fact that the total duration time of $HNSO_2$ at the interface approximately accounts for 49.1 % of the 150 ns simulation time (Fig. S1 in the Supplement). However, the hydrolysis of $HNSO_2$ with MSA has not been studied at the air–water interface, which will limit our understanding of how the hydrolysis of $HNSO_2$ with MSA differs in the gas phase and air–water interfaces.

From a structural point of view, two functional groups of $-NH_2$ and $-SO_3H$ in the SFA molecule can act as both hydrogen donors and acceptors to interact with atmospheric species. Previous studies have demonstrated that SFA has a potential role in new particle formation (NPF), as it not only clusters efficiently with itself and SA (Lovejoy and Hanson, 1996) but can also promote the nucleation rate of NPF initiated from SA-DMA by a factor of 2 in dry and severely contaminated areas with NH_3 (Li et al., 2018). Due to the concentration of SA in the atmosphere decreasing significantly with the scenario of SO_2 emission control measures, MSA-driven NPF has attracted growing attention (Dawson et al., 2012; Nishino et al., 2014; Chen and Finlayson-Pitts, 2017; Chen et al., 2020; Shen et al., 2020). Initially, the binary nucleation of MSA with inorganic ammonia and organic amines in the atmosphere was reported, where MA exhibits the strongest enhancing capability (Chen et al., 2016; Chen and Finlayson-Pitts, 2017; Shen et al., 2019; Hu et al., 2023). Subsequently, some reported results suggest that the

triadic MSA-MA-driven NPF can exhibit greater nucleation rates competed to the binary of MSA-driven NPF (Zhang et al., 2022a: Hu et al., 2023). For example, both formic acid (Zhang et al., 2022a) and trifluoroacetic acid (Hu et al., 2023) exhibit an excellent catalytic influence on MSA-MA-driven NPF. However, the SFA involved in MSA-MA-driven NPF has not been investigated, so it is important to investigate whether SFA can exhibit a similar enhancing effect in MSA-MA to that observed in SA-DMA.

This work studied the catalytic effect of SFA on $HNSO_2$ hydrolysis and MSA-MA nucleation particle formation. Specifically, quantum chemical calculations were used firstly to assess the atmospheric processes of the gaseous hydrolysis of $HNSO_2$ with MSA. Then, the gaseous and interfacial mechanism differences in the $HNSO_2$ hydrolysis with MSA were investigated applying the Born–Oppenheimer molecular dynamics (BOMD) simulation method. Finally, the atmospheric implications and mechanism of SFA in the MSA-MA-dominated NPF process were evaluated density functional theory and Atmospheric Cluster Dynamic Code (ACDC) (McGrath et al., 2012; Hu et al., 2023; Zhao et al., 2020; Zhang et al., 2024; Tsona Tchinda et al., 2022; Liu et al., 2021b) to evaluate the potential effect of SFA on nucleation and NPF. This work will not only deepen our understanding of the source of SFA but also reveal significant implications for new particle formation and aerosol particle growth in MSA-polluted areas.

2 Methodology

2.1 Quantum chemical calculations

The gaseous hydrolysis of $HNSO_2$ with MSA was comprehensively studied through quantum chemistry simulations. Optimization of all the species was carried out by using the method of M06-2X with a 6-311++G(2df,2pd) basis set (Zhao and Truhlar, 2008; Elm et al., 2012; Bork et al., 2014b). Vibrational frequencies were subsequently computed at the M06-2X/6-311++G(2df,2pd) level to ensure the reality of all stationary points' frequencies and the presence of only one imaginary frequency in transition states. It is noted that the calculated bond distances and bond angles at the M06-2X/6-311++G(2df,2pd) level (Fig. S2) agree well with the available values (Fig. S2) from the experiment and three different theoretical levels of the M06-2X/6-311++G(3df,2pd), M062X/6-311++G(3df,3pd), and M06-2X/aug-cc-pVTZ levels. Also, at the M06-2X/6-311++G(2df,2pd) level, internal reaction coordinate (IRC) analyses were conducted to verify the connection from the transition states to the corresponding products (or reactants). All calculations regarding geometries and frequency were conducted with the aid of the Gaussian 09 (Frisch et al., 2009) program. Furthermore, single-point energies were performed at the CCSD(T)-F12/cc-pVDZ-F12 (Kendall et al., 1992; Adler et al., 2007) level utilizing the ORCA (Neese, 2012) program, based on the optimized geometries mentioned above. The CCSD(T)/aug-cc-pVDZ method was chosen to calculate the relative energies as the fact that, compared with unsigned error (Table S1 in the Supplement) calculated at the CCSD(T)/CBS//M06-2X/6-311++G(2df,2pd) level, unsigned errors calculated at CCSD(T)-F12/cc-pVDZ-F12//M06-2X/6-311++G(2df,2pd) were 0.71 kcal mol^{-1}.

2.2 Rate coefficient calculations

The rate coefficients for the hydrolysis of $HNSO_2$ with MSA were calculated through a two-step process. Initially, the high-pressure-limit (HPL) rate coefficients were computed applying VRC-VTST methods within the Polyrate package (Chuang et al., 1999). It is worth noting that the electronic structure method for VRC-TST calculations is based on the Gaussian 09 program using M06-2X/6-311++G(2df,2pd). Meanwhile, two pivot points were selected (Bao et al., 2016; Long et al., 2021; Georgievskii and Klippenstein, 2003; Meana-Pañeda et al., 2024) to produce a single-faceted dividing surface for the $HNSO_2$ hydrolysis (shown in Sect. S1 in the Supplement). Subsequently, on the basis of the HPL rate coefficients, the rate coefficients for the hydrolysis of $HNSO_2$ with MSA were calculated within the temperature range of 212.6–320.0 K and pressures applying the Master Equation Solver for Multi-Energy well Reactions (MESMER) program (Glowacki et al., 2012). The rate coefficients for the barrierless steps transitioning between reactants and pre-reactive complexes were assessed applying the inverse Laplace transform (ILT) method within MESMER calculations, while the step-transitioning between pre-reactive complexes and post-reactive complexes via transition states was evaluated using the RRKM theory (Mai et al., 2018) in combination with the asymmetric Eckart model. The details of the rate coefficient for the hydrolysis of $HNSO_2$ with and without X ($X = H_2O$ and MSA) are given in Sect. S1 and Tables 1 and S4.

2.3 BOMD simulations

BOMD simulations were conducted applying DFT implemented in the CP2K program (VandeVondele et al., 2005; Hutter et al., 2014). The exchange and correlation interactions were addressed using the Becke–Lee–Yang–Parr (BLYP) functional (Becke, 1988; Lee et al., 1988), while Grimme's dispersion was applied to address weak dispersion interaction (Grimme et al., 2010). The Goedecker–Teter–Hutter (GTH) conservation pseudopotential (Goedecker et al., 1996; Hartwigsen et al., 1998), combined with a Gaussian DZVP basis set (VandeVondele and Hutter, 2007) and an auxiliary plane wave basis set, was used to represent core and valence electrons. Energy cutoffs (Zhong et al., 2017, 2018, 2019) of 280 Ry for the plane wave basis set and 40 Ry for the Gaussian basis set were applied. The gaseous reactions were simulated in the NVT ensemble at 300 K, with

$15 \times 15 \times 15$ Å^3 supercells and a time step of 1 fs. To simulate the water microdroplet, the system containing 191 water molecules (Zhong et al., 2017) was utilized in $35 \times 35 \times 35$ Å^3 supercells. This setup included $HNSO_2$ and MSA along with the water drop. Prior to the interfacial simulation, a 10 ps relaxation period in the BOMD simulation was used to equilibrate the water microdroplet system with 191 molecules.

2.4 ACDC kinetics simulation

The ACDC model (McGrath et al., 2012; Hu et al., 2023; Zhao et al., 2020; Zhang et al., 2024; Tsona Tchinda et al., 2022; Liu et al., 2021b) was utilized to simulate the $(MSA)_x(MA)_y(SFA)_z$ ($0 \le y \le x + z \le 3$) cluster formation rates and explore the potential mechanisms, where the most stable structures of $(SFA)_x(MSA)_y(MA)_z$ ($0 \le z \le x + y \le 3$) clusters were searched with ABCluster software (Zhang and Dolg, 2015) (the details are in Sect. S1). This simulation encompasses a variety of temperatures and monomer concentrations to capture the dynamics under different environmental conditions. Thermodynamic parameters, obtained from quantum chemical calculations executed at the M06-2X/6-311++G(2df,2pd) level, were used as inputs for the ACDC model. Notably, many benchmark studies (Zhao et al., 2020; Zhang et al., 2024; Tsona Tchinda et al., 2022; Liu et al., 2021b) show that the M06-2X functional has good performance compared to other common functionals for gaining the Gibbs free energies. For all the M06-2X calculations, the 6-311++G(2df,2pd) basis set was used, as it is a good compromise between accuracy and efficiency and does not yield significant errors in the thermal contribution to the free energy compared to much larger basis sets, such as 6-311++G(3df,3pd), with differences in relative ΔG less than 1.75 kcal mol^{-1} (Table S7). The temporal progression of cluster concentrations was determined by numerically integrating the birth–death equation, leveraging MATLAB's ode15s solver for enhanced accuracy.

$$\frac{dc_i}{dt} = \frac{1}{2}\sum_{j<i}\beta_{j,(i-j)}c_j c_{(i-j)} + \sum_j \gamma_{(i+j)\to i}c_{i+j} - \sum_j \beta_{i,j}c_i c_j - \frac{1}{2}\sum_{j<i}\gamma_{i\to j}c_i + Q_i - S_i \quad (2)$$

Here, c_i represents the concentration of a specific cluster, labeled as i; the term $\beta_{i,j}$ was used to denote the collision coefficient, which was a measure of the frequency at which clusters i and j collide with each other in a given environment or system; the coefficient $\gamma_{(i+j\to i)}$ was defined as the evaporation rate constant that describes the process of a larger cluster, consisting of combined elements i and j, breaking down into the individual smaller clusters i and j; and Q_i encompasses all other source terms contributing to the formation of cluster i. S_i signifies alternative sink terms for cluster i that may remove it from the system. Considering the formation Gibbs free energy (Table S8) and evaporation

Table 1. Rate coefficients (k, cm^3 molec.$^{-1}$ s^{-1}) and effective rate constants (k', cm^3 molec.$^{-1}$ s^{-1}) for the hydrolysis of $HNSO_2$ with H_2O and MSA calculated by the master equation within the temperature range of 213–320 K and altitude range of 0–15 km.

Altitude		0 km					5 km	10 km	15 km
T/K		280	290	298	300	310	320	259.3	229.7	212.6
k_{WM}		7.64×10^{-13}	6.45×10^{-13}	5.63×10^{-13}	5.44×10^{-13}	4.59×10^{-13}	3.88×10^{-13}	1.09×10^{-12}	1.72×10^{-12}	2.22×10^{-12}
k_{MSA}		3.08×10^{-11}	2.96×10^{-11}	2.85×10^{-11}	2.82×10^{-11}	2.67×10^{-11}	2.52×10^{-11}	3.32×10^{-11}	3.49×10^{-11}	03.5×10^{-11}
k'_{WM}	20 % RH	5.99×10^{-18}	7.96×10^{-18}	9.64×10^{-18}	1.03×10^{-17}	1.29×10^{-17}	1.36×10^{-17}			
	40 % RH	1.19×10^{-17}	1.58×10^{-17}	1.99×10^{-17}	2.07×10^{-17}	2.60×10^{-17}	3.12×10^{-17}			
	60 % RH	1.79×10^{-17}	2.38×10^{-17}	2.98×10^{-17}	3.11×10^{-17}	3.90×10^{-17}	4.68×10^{-17}	9.85×10^{-27}	1.71×10^{-22}	6.51×10^{-22}
	80 % RH	2.39×10^{-17}	3.17×10^{-17}	3.97×10^{-17}	4.14×10^{-17}	5.21×10^{-17}	6.24×10^{-17}			
	100 % RH	2.97×10^{-17}	3.96×10^{-17}	4.97×10^{-17}	5.18×10^{-17}	6.50×10^{-17}	7.79×10^{-17}			
k'_{MSA}	$[MSA] = 10^8$	4.81×10^{-19}	2.50×10^{-19}	1.57×10^{-19}	1.40×10^{-19}	7.90×10^{-20}	4.60×10^{-20}	1.96×10^{-20}	2.37×10^{-19}	1.30×10^{-18}
k'_{MSA}/k'_{WM}		1.62×10^{-4}	6.42×10^{-5}	3.16×10^{-5}	2.69×10^{-5}	1.22×10^{-5}	5.90×10^{-5}	3.01×10^{1}	1.38×10^{3}	1.32×10^{8}

k_{WM} and k_{MSA} are respectively the rate constants for the hydrolysis of $HNSO_2$ with H_2O and MSA; k'_{WM} and k'_{MSA} are respectively the effective rate constants for the hydrolysis of $HNSO_2$ with H_2O and MSA.

rates (Table S9) of all clusters, the clusters containing pure MSA and MA molecules and the clusters containing an SFA molecule are mostly more stable and therefore are allowed to form larger clusters and contribute to particle formation rates. In this case, clusters $(MSA)_4 \cdot (MA)_3$, $(MSA)_4 \cdot (MA)_4$ and SFA
,$\cdot (MSA)_3 \cdot (MA)_3$ are set as the boundary clusters.

3 Results and discussion

3.1 The hydrolysis of $HNSO_2$ with MSA in the gas phase

Given the low chance of three molecules of $HNSO_2$, H_2O, and MSA colliding simultaneously under atmospheric conditions, the hydrolysis of $HNSO_2$ with MSA (Channel MSA) was likely a sequential bimolecular process. As the concentration of water molecules (10^{18} molec. cm^{-3}; Anglada et al., 2013) in the atmosphere is much higher than that of $HNSO_2$ and MSA (10^5–10^9 molec. cm^{-3}; Shen et al., 2020), it is hard for the reaction pathway of $HNSO_2 \ldots MSA + H_2O$ to occur in actual atmospheric conditions. Therefore, Channel MSA proceeds through the initial formation of dimers ($HNSO_2 \ldots H_2O$ and $MSA.\ldots H_2O$) via collisions between $HNSO_2$ (or MSA) and H_2O. Subsequently, the generated dimer interacts with the third reactant, either MSA or $HNSO_2$. As seen in Fig. 1, the calculated Gibbs free energy of the $MSA \ldots H_2O$ complex was -0.9 kcal mol^{-1}, which was 4.5 kcal mol^{-1} lower than that of $HNSO_2 \ldots H_2O$. Consequently, it was predicted that the primary route for the hydrolysis reaction of $HNSO_2$ with MSA takes place via the $HNSO_2 + MSA \ldots H_2O$ reaction.

Starting from the $HNSO_2 + MSA \ldots H_2O$ reactants, Channel MSA was initiated through the intermediate complex designated as IM_MSA1. From a geometric perspective, the IM_MSA1 complex exhibits a cage-like configuration by a van der Waals (vdW) force ($S_1 \ldots O_1$, 2.00 Å) and the involvement of three hydrogen bonds: $H_2 \ldots O_4$ (1.53 Å), $H_4 \ldots N_1$ (1.60 Å), and $H_5 \ldots O_3$ (2.07 Å). The Gibbs free energy of the IM_MSA1 complex relative to $HNSO_2 + MSA \ldots H_2O$ reactants was 1.7 kcal mol^{-1}. Subsequently, as presented in Fig. 1, Channel MSA progresses through the transition state TS_MSA1 to yield complex IMF_MSA1. At TS_MSA1, the MSA moiety facilitates two hydrogen atom transfers, with TS_MSA1 lying only 0.8 kcal mol^{-1} above complex IM_MSA1. Complex IMF_MSA1 exhibits a cage-like structure with a Gibbs free energy 23.4 kcal mol^{-1} lower than that of IM_MSA1, revealing thermodynamic favorability of $HNSO_2$ hydrolysis with MSA. To evaluate the relative catalytic impact of MSA and H_2O, Fig. S4 illustrates the profiles of Gibbs free energy for the hydrolysis of $HNSO_2$ and the corresponding reaction assisted by H_2O. Compared to complex $HNSO_2 \ldots (H_2O)_2$, the Gibbs stabilization energy of IM_MSA1 increased by 5.6 kcal mol^{-1}, potentially shortening the $S_1 \ldots O_1$ bond distance by 0.21 Å. Considering the Gibbs free energy barrier and rate coefficients, MSA demonstrates a greater catalytic role compared to H_2O in lowering the energy barrier for the hydrolysis of $HNSO_2$. In particular, MSA facilitates the hydrogen atom to extraction from H_2O, further reducing the reaction energy barriers to 7.7 kcal mol^{-1}. Meanwhile, the calculated rate coefficients for $HNSO_2$ hydrolysis with MSA were 3.08×10^{-11}–3.50×10^{-11} cm^3 molec.$^{-1}$ s^{-1} within 212.6–320.0 K, exceeding corresponding values for reactions involving H_2O by 2 orders of magnitude. Besides, the Gibbs free energy of IMF_MSA1 was 2.0 kcal mol^{-1} lower than that of the product complex IMF_WM1 ($SFA \ldots H_2O$), suggesting SFA has a higher affinity for MSA compared to H_2O. Besides, MSA-assisted $HNSO_2$ hydrolysis is reduced by 4.9 kcal mol^{-1} in the energy barrier, as opposed to the NH_3-assisted ammonolysis of SO_3, with its rate constant at 298 K (2.85×10^{-11} cm^3 molec.$^{-1}$ s^{-1}) close to the value of ammonolysis of SO_3 with NH_3 (4.35×10^{-10} cm^3 molec.$^{-1}$ s^{-1}) (Li et al., 2018). However, due to the absence of the concentration of $HNSO_2$, the competitiveness of these two reactions cannot be further confirmed.

To evaluate the comparative catalytic ability of X ($X = H_2O$ and MSA) in the atmosphere, the effective rate coefficients (k') for X-assisted $HNSO_2$ hydrolysis were calculated in Table 1. Notably, k' serves as a metric for gauging the comparative catalytic ability of a series of gaseous catalysts in atmospheric reactions (Sarkar et al., 2017; Zhang et al., 2019, 2020; Buszek et al., 2012; Gonzalez et al., 2011; Parandaman et al., 2018; Anglada et al., 2013). When X was present, the calculated k' was given by Eq. (3).

$$k'X = k_X \times K_{eq}(X \ldots H_2O) \times [X] \quad (3)$$

In Eq. (3), k_X was the rate coefficient for X-assisted $HNSO_2$ hydrolysis (Table 1), while K_{eq} ($X \ldots H_2O$) denotes the equilibrium coefficients of $X \ldots H_2O$ (Table S2). $[X]$ represents the available concentrations of H_2O (Anglada et al., 2013) and MSA (Shen et al., 2020). As indicated in Table 1, at experimental concentrations ($[H_2O] = 5.16 \times 10^{16}$–$2.35 \times 10^{18}$ molec. cm^{-3}) within 280.0–320.0 K (at 0 km), the computed k'_{WM} ranged from 5.99×10^{-18}–7.79×10^{-17} cm^3 molec.$^{-1}$ s^{-1}. This range exceeded k'_{MSA} (4.60×10^{-21}–4.81×10^{-20} cm^3 molec.$^{-1}$ s^{-1}) by 2–4 orders of magnitude, highlighting the pronounced impact of H_2O compared to MSA at 0 km in enhancing the rate of $HNSO_2$ hydrolysis. However, with the significant decrease in atmospheric water molecules with increasing altitude, the calculated k'_{MSA} ranged from 1.96×10^{-19} s^{-1}–1.30×10^{-17} cm^3 molec.$^{-1}$ s^{-1}, surpassing k'_{WM} (9.85×10^{-27}–6.51×10^{-22} cm^3 molec.$^{-1}$ s^{-1}) by 3–10 orders of magnitude. This illustrates that MSA has a significantly greater catalytic ability than H_2O in accelerating the rate of $HNSO_2$ hydrolysis within 5–15 km. So, $HNSO_2$ hydrolysis with MSA may represent a potential formation pathway for SFA across an altitude scope of 5–15 km.

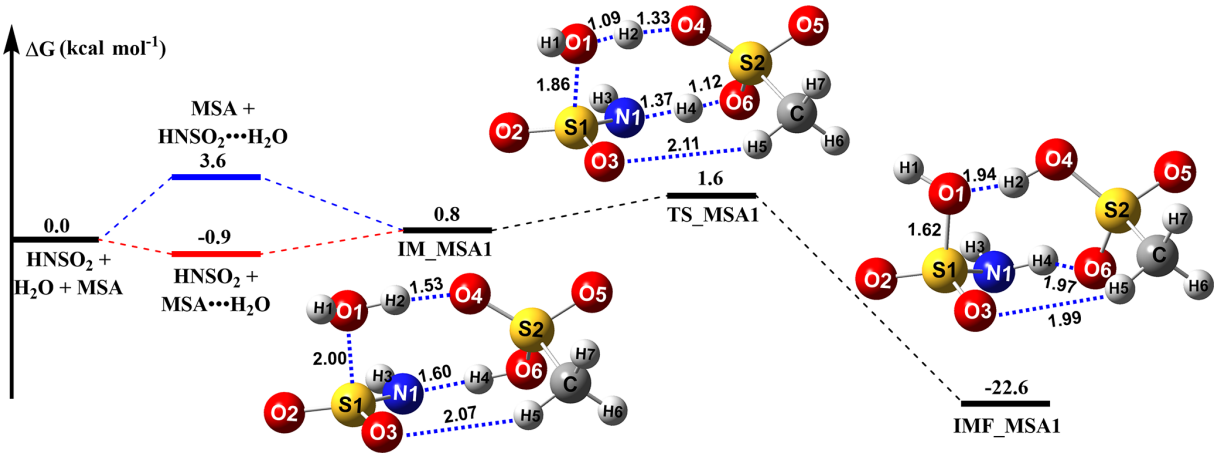

Figure 1. The potential energy profile (ΔG) for the hydrolysis reaction of $HNSO_2$ with MSA at the CCSD(T)-F12/cc-pVDZ-F12//M06-2X/6-311++G(2df,2pd) level of theory.

3.2 Reactions at the air–water interface

The interfacial mechanism of MSA-assisted $HNSO_2$ hydrolysis at the air–water interface has not been thoroughly investigated. Interestingly, our simulations show that $HNSO_2$ and MSA molecules spend approximately 49.1 % and 12.1 % of the time, respectively, at the air–water interface during the 150 ns simulation (Figs. S1 and S6). This reveals that the presence of $HNSO_2$ and MSA at the air–water interface should not be disregarded. Therefore, BOMD simulations were performed to clarify the interfacial mechanism of MSA-assisted $HNSO_2$ hydrolysis at the air–water interface. Comparable to the reactions of SO_3 at the air–water interface with acidic molecules (Cheng et al., 2023; Zhong et al., 2019), the hydrolysis of $HNSO_2$ with MSA at the air–water interface may occur through three pathways: (i) the adsorbed MSA interacts with $HNSO_2$ at the air–water interface, (ii) the adsorbed $HNSO_2$ interacts with MSA at the air–water interface, and (iii) the $HNSO_2 \ldots$ MSA complex reacts at the air–water interface. Nevertheless, because of the high reactiveness of MSA at the air–water interface, the lifetime of MSA was minimal (seen in Fig. S9) on the water droplet, which was around a small number of picoseconds, leading to the rapid formation of MSA^- ion. Meanwhile, although $HNSO_2$ remains stable at the air–water interface (seen in Fig. S8) and does not dissociate within 10 ps, the hydrated form of $HNSO_2$ illustrated in Fig. S8 was not conducive to $HNSO_2$ hydrolysis at the air–water interface. Therefore, model (iii) was primarily considered for $HNSO_2$ hydrolysis with MSA at the air–water interface. It is worth noting that the $HNSO_2 \ldots$ MSA complex can persist at the air–water interface for approximately 34.2 % of the 150 ns simulation time (see in Fig. S7). For model (iii), two types of reactions were found at the air–water interface: (a) the $NH_2SO_3^-$ and H_3O^+ ion formation mechanism and (b) the proton exchange mechanism.

$NH_2SO_3^-$ and H_3O^+ ion formation mechanism. Figures 2a and S10 and Movie S1 illustrate the formation mechanism of $NH_2SO_3^-$ and H_3O^+ ions through the chain structure at 4.57 ps, and a chain-hydrolyzed transition state was observed, accompanied by two proton transfer events. IN particular, an H_2 atom transferred from the OH moiety of an MSA molecule to the terminal N atom of an $HNSO_2$ molecule, resulting in the breaking of the O_3–H_2 bond (with a length of 1.49 Å) and the formation of an H_2–N bond (with a length of 1.14 Å). Concurrently, an interfacial water molecule decomposes, leading to the elongation of the O_1–H_1 bond to over 1.00 Å, with the S1 atom of $HNSO_2$ obtaining the OH moiety of the interfacial water molecule ($d_{(S_1-O_1)} = 1.60$ Å). By 4.61 ps, the N–H_2 and S_1–O_1 bonds both shortened to 0.99 and 1.01 Å, revealing the formation of the SFA molecule. However, due to its strong acidity, the SFA molecule could only persist on the water droplet surface for a picosecond timescale. As a result, at 7.43 ps, the proton of SFA transferred to another interfacial water molecule, completing the deprotonation of SFA. The loop structure mechanism (Figs. 2b and S11 and Movie S2) was similar to the chain structure mechanism. However, in this case, the proton of SFA transferred to $CH_3SO_3^-$ rather than to an interfacial water molecule.

Proton exchange mechanism. As depicted in Fig. 3, the proton exchange mechanism illustrates the deprotonation of MSA concurrent with $HNSO_2$ hydration at the air–water interface. As shown in Figs. 3a and S12 and Movie S3, MSA-mediated $HNSO_2$ hydration with a single water molecule was observed. Initially, the $HNSO_2 \ldots$ MSA complex quickly associates with an interfacial water molecule and forms a loop structure complex that accelerates the rate of proton transfer. By 4.38 ps, an eight-membered loop structure complex, $HNSO_2 \ldots H_2O \ldots$ MSA, emerges, characterized by two hydrogen bonds ($d_{(H_2-N)} = 1.82$ Å and $d_{(H_1-O_2)} = 1.92$ Å) and a van der Waals force ($d_{(S_1-O_1)} =$

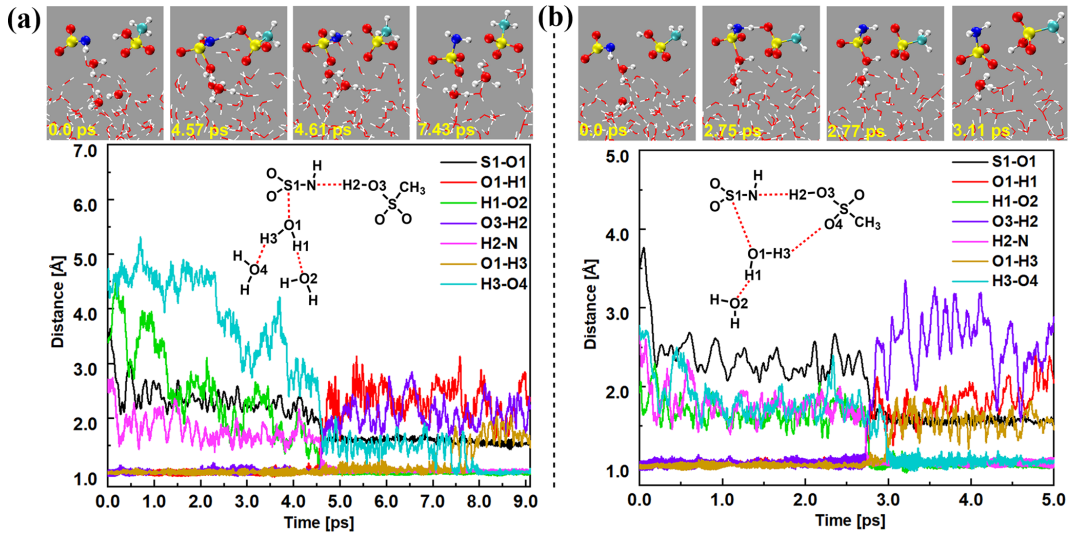

Figure 2. BOMD simulation trajectories and snapshots of the $NH_2SO_3^-$ and H_3O^+ ion formation mechanism – chain structure **(a)** and loop-structure **(b)** – in the $HNSO_2$ hydrolysis with MSA at the air–water interface.

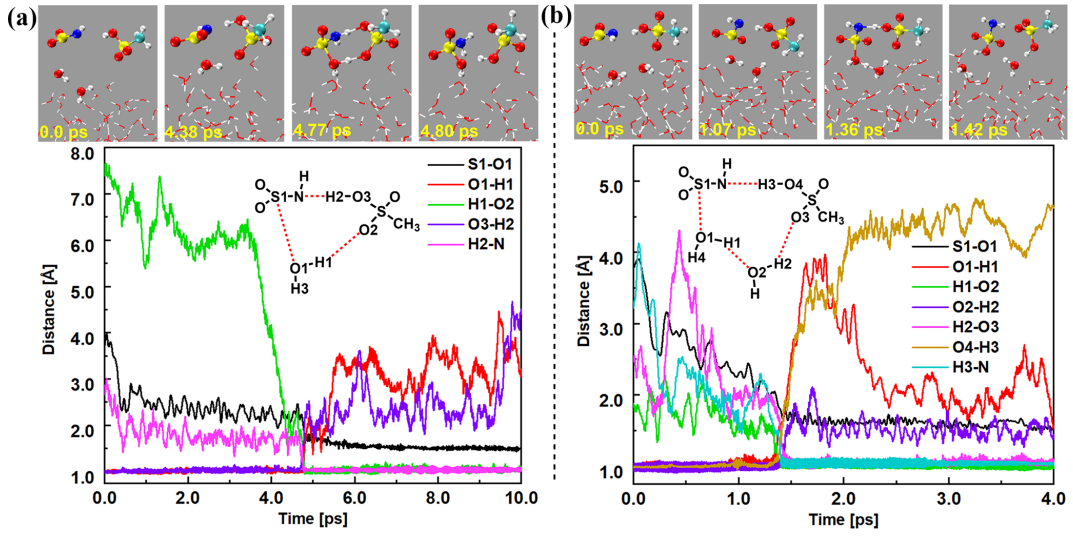

Figure 3. BOMD simulation trajectories and snapshots of the proton exchange mechanism in MSA-mediated $HNSO_2$ hydration with one **(a)** and two **(b)** water molecules at the air–water interface.

2.35 Å). Thereafter, at 4.77 ps, a transition-state-like configuration was identified where the water molecule within the loop complex dissociated, elongating the O_1–H_1 bond to over 1.00 Å, and the S atom of $HNSO_2$ attached to the OH group of the interfacial water molecule. Concurrently, the $CH_3SO_3^-$ ion receives the proton from the separated interfacial water molecule. The entire reaction for MSA-mediated $HNSO_2$ hydration with one water molecule was completed at 4.80 ps, resulting in the formation of SFA and MSA molecules. MSA-mediated hydration of $HNSO_2$ with two water molecules (Figs. 3b and S13 and Movie S4) at the air–water interface was similar to the mechanism identified with one water molecule. However, the inclusion of two water molecules enlarges the loop, significantly reducing the stress on the loop structures. Consistent with the prediction in Fig. 4, the loop structures preferred to include two water molecules rather than one water molecule. This observation agrees well with the reported hydration of the Criegee intermediate at the air–water interface (Zhu et al., 2016; Kumar et al., 2018; Liu et al., 2021a; Zhang et al., 2023a). Additionally, MSA-mediated hydration of $HNSO_2$ with three water molecules (Fig. S14 and Movie S5) was observed in the proton exchange mechanism. However, its probability of occurrence was smaller due to the relatively larger entropy effect. It was noteworthy that the SFA and MSA molecules formed in the proton exchange mechanism were not stable at the air–

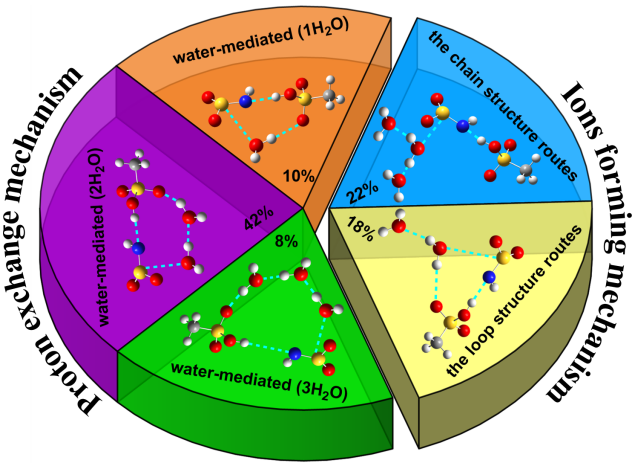

Figure 4. Percentages of different mechanisms for $HNSO_2$ hydrolysis with MSA at the air–water interface observed in BOMD simulations.

water interface, which can further interact with an interfacial water molecule to form the corresponding ions of $NH_2SO_3^-$ and $CH_3SO_3^-$.

At the air–water interface, a sum of 50 BOMD trajectories, each lasting 10 ps, was conducted to investigate $HNSO_2$ hydrolysis with MSA. Two distinct mechanisms were observed: the formation of $NH_2SO_3^-$ and H_3O^+ ions (shown in blue and yellow in Fig. 4) and the proton exchange mechanism (represented by orange, purple, and green in Fig. 4). In the mechanism involving the formation of $NH_2SO_3^-$ and H_3O^+ ions, approximately 22 % (Figs. 2a, 4, and S10 and Movie S1) of the reactions took place via a chain structure, while the majority ($\sim$ 18 %) (Figs. 2b, 4, and S11 and Movie S2) proceeded through a loop structure mechanism. This discrepancy can be attributed to the uncertainty regarding the direction of proton transfer from SFA. Since the number of water molecules near the water microdroplet far exceeded that of $CH_3SO_3^-$, protons were predominantly transferred to interface water molecules, making the loop structure mechanism weaker than the chain structure mechanism. Approximately 60 % of the reactions were observed to be due to the proton exchange mechanism in BOMD simulations. Through water-mediated mechanisms, these reactions resulted in SFA formation. Similarly to gas-phase reactions, loop structures were observed in these reactions. Approximately 10 % of the reactions formed a loop structure involving one water molecule (Figs. 3a, 4, and S12 and Movie S3), while the most common loop structure involved two water molecules (about 42 %) (Figs. 3b, 4, and S13 and Movie S4). Smaller loops were found to experience more stress than loop structures with two water molecules. In cases of loop structures with three water molecules (about 8 %) (Figs. 4 and S14 and Movie S5), the entropy effect was deemed to be more significant than the strain effect and likely played a dominant role. The two water molecules contained in the loop structure not only acted as a reactant but also facilitated proton transfer as a bridge.

3.3 New particle formation from the atmospheric products

3.3.1 The influence of SFA on the stability of atmospheric MSA-MA-based clusters

Electrostatic potential (ESP) mapping on the molecular van der Waals (vdW) surface was employed to analyze the interactions between SFA and other key nucleation precursors like MSA and MA. As shown in Fig. 5, sites with more negative ESP often attract more positive ESP sites, namely hydrogen bonds in the studied system. Specifically, the hydrogen atoms of the $-SO_3H$ and $-NH_2$ groups (site 4 and 5) in SFA, possessing more positive ESP values, have the potential to attract groups with negative ESP values, such as the oxygen atom within the $-SO_3H$ group of MSA (site 6) and the nitrogen atom of MA (site 1), thus forming hydrogen bonds as proton donors. Additionally, the sulfur atom of the $-SO_3H$ functional group (site 7) in SFA, with a negative ESP of -30.75, acts as proton acceptor, facilitating direct binding with MSA and MA molecules via the hydrogen bonds. Therefore, the introduction of SFA was believed to enhance the stability of MSA-MA clusters by promoting the formation of more hydrogen bonds and facilitating proton transfers.

3.3.2 The cluster formation rates in the SFA-MSA-MA system

Simulations were conducted to determine the cluster formation rates (J) for the MSA-MA-SFA system, with varying parameters such as temperature and the concentrations of the precursors involved. To assess the promotional impact of SFA on J under varying atmospheric conditions, the enhancement factor (R) was computed as the ratio of $J_{\text{MSA-MA-SFA}}$ to $J_{\text{MSA-MA}}$. As depicted in Fig. 6a, the J of the MSA-MA-SFA system exhibits a negative correlation with temperature, attributed to the decrease in ΔG value and evaporation rates of clusters at lower temperatures. Conversely, a positive correlation of R with temperature was observed (Fig. 6b), indicating that SFA's enhancement of nucleation was more pronounced in regions with relatively higher temperatures. Furthermore, both J and R show an increase as the [SFA] increases, suggesting a positive correlation of J and R with [SFA]. In short, in regions with high [SFA], such as the Yangtze River Delta of China, Bangladesh, and the east coast of India, SFA was expected to significantly boost the J of MSA-MA-based nucleation. It is noted that, in Fig. 6b, due to the competitive relationship between MSA and SFA, at low concentrations of SFA, the binding capacity of MSA with MA is stronger than that of SFA with MA, resulting in only a small amount of SFA participating in cluster formation. However, as the concentration of SFA increases, the

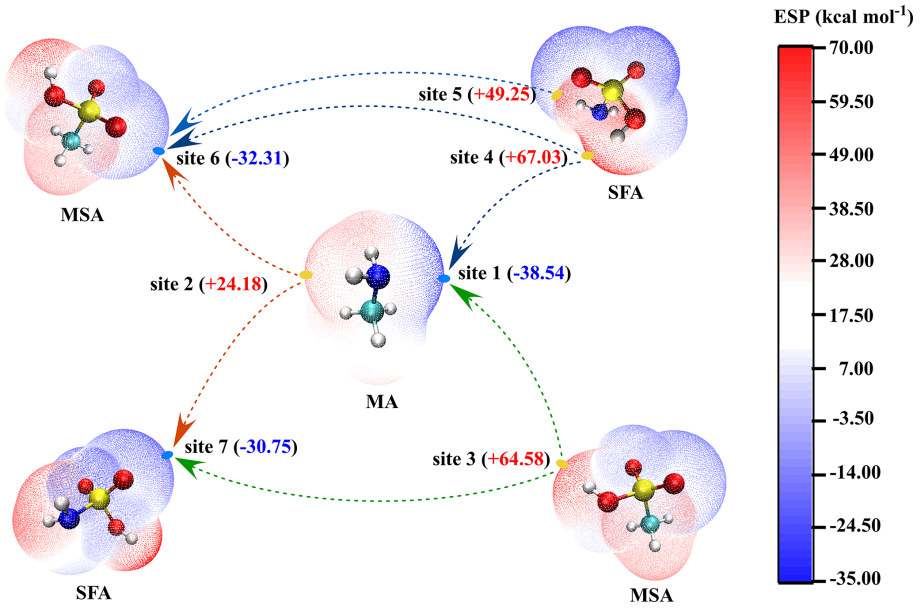

Figure 5. ESP-mapped molecular vdW surface of MA, SFA, and MSA molecules at the M06-2X/6-311++G(2df,2pd) level of theory. Surface local minima and maxima of ESP of the different functional groups in MA, SFA, and MSA molecules are represented as blue and yellow spheres, respectively. The values of maximum and minimum are shown in kcal mol^{-1} in the parentheses. The green, red, and blue arrows refer to the tendencies to form hydrogen bonds and proton transfer events, respectively (green: carbon; red: oxygen; blue: nitrogen; yellow: sulfur; and white: hydrogen).

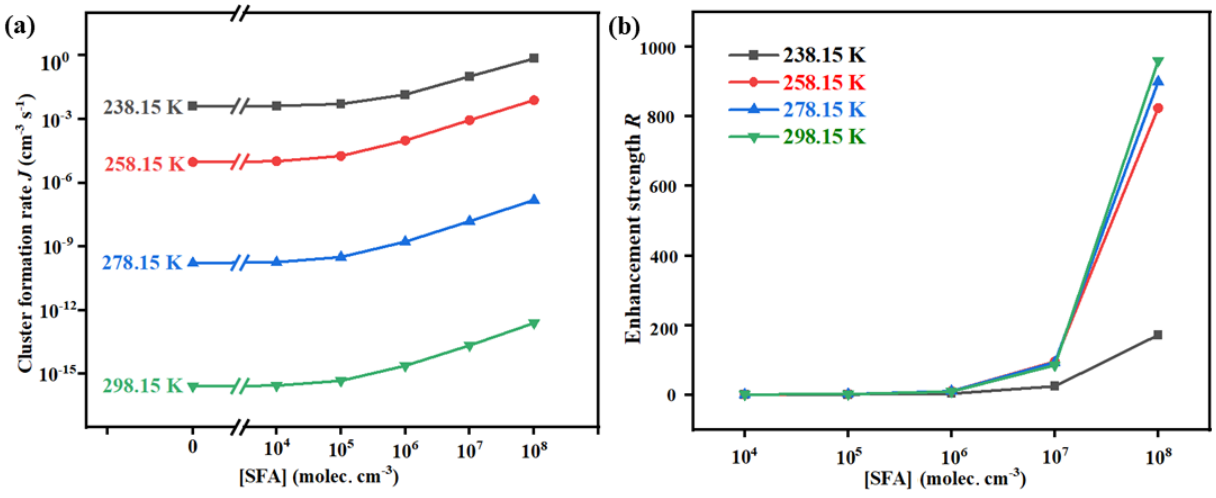

Figure 6. The J (cm^{-3} s^{-1}) (**a**) and R (**b**) versus [SFA] with [MSA] = 10^6 molec. cm^{-3}, [MA] = 2.5×10^8 molec. cm^{-3}, and four different temperatures (green line: 298.15 K; blue line: 278.15 K; red line: 258.15 K; black line: 238.15 K).

number of $(MSA)_x \cdot (MA)_y \cdot (SFA)_z$ (where $y \leq x + z \leq 3$) ternary clusters increases, leading to the formation of more hydrogen bonds and a significant increase in R_{SFA}. Additionally, Fig. 7 illustrates the J and R of MSA-MA-SFA clusters under different [MSA] and [MA]. On the one hand, larger values of [MSA] and [MA] correspond to higher J, as the increased concentration of nucleation precursors leads to a rise in the number of MSA-MA-FSA clusters. On the other hand, increasing [MSA] and [MA] result in a decrease in the R attributed to the effect of SFA on nucleation. This was because, as [MSA] and [MA] increase, the prevalence of pure MSA-MA clusters rises during the clustering process, consequently reducing the impact of SFA.

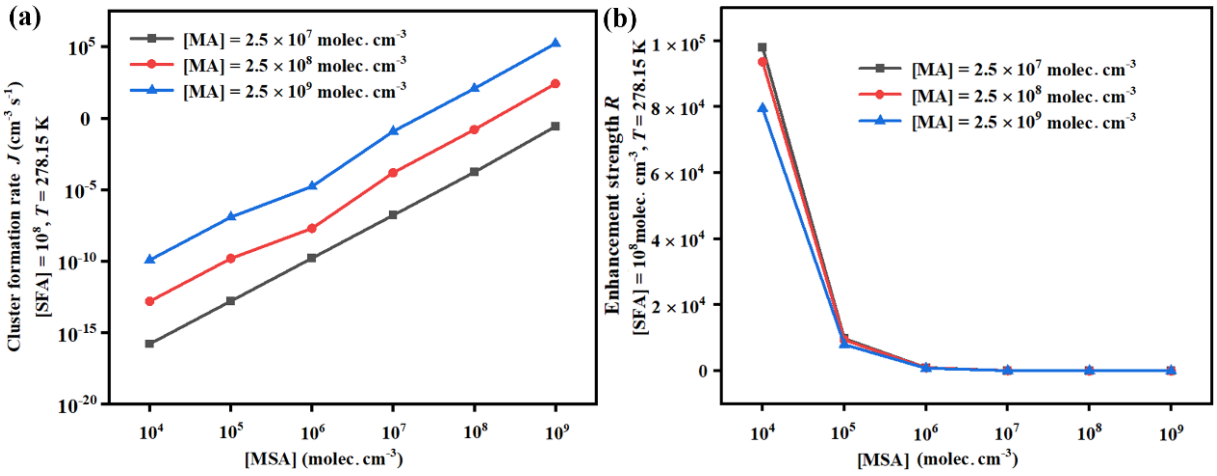

Figure 7. The J ($cm^{-3}\,s^{-1}$) **(a)** and R **(b)** as a function of [MSA] with [SFA] = 10^8 molec. cm^{-3} and three different [MA] (black line: [MA] = 2.5×10^7 molec. cm^{-3}; red line: [MA] = 2.5×10^8 molec. cm^{-3}; blue line: [MA] = 2.5×10^9 molec. cm^{-3}) at 278.15 K.

3.3.3 The growth paths of clusters under different atmospheric conditions

Li et al. (2018) studied the atmospheric concentration of SFA estimated by the theoretical method (Li et al., 2018) and expected it to reach up to 10^8 molec. cm^{-3} in high NH_3 concentrations, such as the Yangtze River Delta in China (Yu et al., 2020), the Indo-Gangetic Plains (Kuttippurath et al., 2020), Pakistan, Bangladesh (Warner et al., 2016), and southern Italy (Tang et al., 2021). Considering the high atmospheric concentrations of MSA and MA detected in coastal industrial areas (Shen et al., 2020; Mao et al., 2018), SFA could be an important contributor to MSA-MA-driven NPF, such as the Yangtze River Delta in China, the east coast of India, the south of Bangladesh, and Italy. To further evaluate the implications of SFA for the MSA-MA nucleation in the atmosphere, the growth paths of clusters were calculated under different atmospheric conditions. In Fig. 8a, two main types of cluster formation routes were found: (i) the pure MSA-MA pathway and (ii) the MSA-MA-SFA pathways at 278.15 K in the studied system. In the pure MSA-MA pathway, cluster growth primarily occurs through the collisional addition of MSA or MA monomers. Conversely, in the SFA-involved pathways, SFA can directly participate in the formation of stable larger clusters, such as $(MSA)_2 \cdot (MA)_2 \cdot SFA$ and $(MSA)_2 \cdot (MA)_2 \cdot (SFA)_2$ clusters, and then subsequently grow out. The involvement of SFA in the cluster formation pathway was significantly influenced by atmospheric conditions. Firstly, as the temperature rises from 238.15 to 278.15 K, the contribution of the SFA-involved cluster formation pathways rises from 68 % to 90 % (Fig. 8b), implying that the pathway involving SFA becomes increasingly important at lower altitudes or in warmer conditions. Secondly, as depicted in Figs. 8c and S22, the contribution of SFA to the MSA-MA system is primarily influenced by [SFA] and [MSA], with negligible dependence on [MA]. To assess the role of SFA in MSA-MA nucleation in the atmosphere, the specific contribution of the MSA-MA cluster growth paths at varying [SFA] to NPF was calculated at 278.15 K, as illustrated in Fig. 8c, under the ambient conditions typical of the corresponding regions. Generally, as [SFA] increases from 10^4 to 10^8 molec. cm^{-3}, the contribution of the SFA-involved pathway increases gradually. Specifically, at low [SFA] (10^4 molec. cm^{-3}), the contributions of SFA-involved clustering pathways are 77 % and 41 % in regions with relatively low [MSA] in non-sea regions (Berresheim et al., 2002). In regions with high [SFA] (10^6, 10^8 molec. cm^{-3}), the contributions of the SFA-MSA-MA growth pathways are dominant in their NPF. Particularly in areas with high [MSA], such as the Pacific Rim (6.26×10^8 molec. cm^{-3}; Saltzman et al., 1986), the central Mediterranean Sea (2.11×10^8 molec. cm^{-3}; Mansour et al., 2020), and the Amundsen Sea (3.65×10^9 molec. cm^{-3}; Jung et al., 2020), nucleation is primarily driven by the SFA-MSA-MA pathway, contributing to approximately 88 % of cluster formation. These results suggest that the influence of SFA is more pronounced in regions with relatively high [MSA]. It is important to note that the [SFA] values discussed in this work are estimated from limited observational data based on the reaction between SO_3 and NH_3 in the atmosphere. Accurate determination of atmospheric [SFA] requires extensive field observations to enable more comprehensive research.

3.4 Interfacial implications of products on aerosol particle growth

As the discussion above, the formation of $SFA^- \ldots H_3O^+$ and $MSA^- \ldots H_3O^+$ ion pairs can occur within a few picoseconds at the air–water interface. The atmospheric affinity of MSA^-, SFA^-, and H_3O^+ for gaseous precursors was further probed by evaluating the free energies of interaction. It was worth noting that compounds such as MSA,

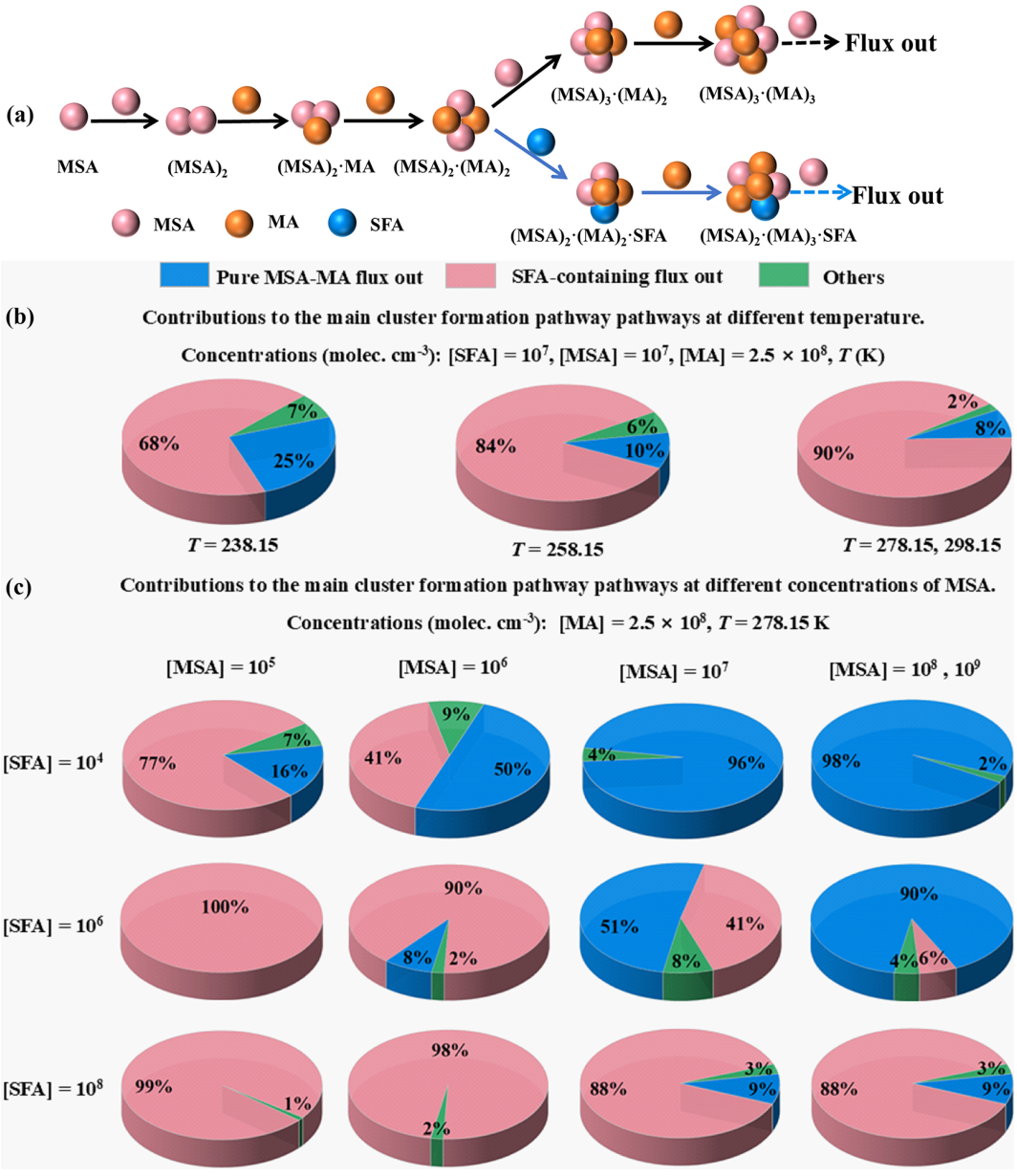

Figure 8. Main cluster formation mechanism of the MSA-MA-SFA-based system at 278.15 K: [MSA] = 10^7 molec. cm^{-3}, [MA] = 2.5 × 10^8 molec. cm^{-3}, and [SFA] = 10^6 molec. cm^{-3}. **(a)** The black arrows indicate the pure MSA-MA-based growth pathways. Blue arrows represent the pathways containing SFA. The influence of **(b)** temperature, **(c)** [SFA], and [MSA] on the relative contribution of the pure MSA-MA-based clustering pathway and the SFA participation pathway to the system flux is analyzed. Other results in panels **(b)** and **(c)** indicate that the pathway contribution of the cluster growing out of the studied system is less than 5 %.

MA, HNO_3 (NA), and $(COOH)_2$ (OA) were identified as candidate species for consideration (Wang et al., 2024; Kulmala et al., 2004). As presented in Table 2, the computed binding energies demonstrate that the interactions of SFA^- ... MSA, SFA^- ... NA, SFA^- ... OA, H_3O^+ ... MA, MSA^- ... MSA, MSA^- ... OA, and MSA^- ... NA were stronger than those of MSA ... MA (one of the primary precursors for atmospheric aerosols), with their Gibbs free energies increased by 14.3–50.9 kcal mol^{-1}. The findings indicate that the presence of SFA^-, MSA^-, and H_3O^+ at the interface facilitates the capture of potential gaseous species onto the surface of the water microdroplet.

Furthermore, we investigated the possibility of SFA^- contributing to the enlargement of particles within the MSA-MA cluster, taking into account the geometric configuration and the free energy of formation for the $(MSA)_1 \cdot (MA)_1 \cdot (SFA^-)_1$ clusters aggregating. Compared with other clusters, such as $(MSA)_1 \cdot (MA)_1 \cdot (X)_1$

(where X = HCOOH, CH_3COOH, CHOCOOH, OA, $CH_3COCOOH$, $HOOCCH_2COOH$, $HOOC(CH)_2COOH$, $HOOC(CH_2)_2COOH$, $HOOC(CH_2)_3COOH$, $C_6H_5(COOH)$, and $C_{10}H_{16}O_3$) clusters (Zhang et al., 2022a), the quantity of hydrogen bonds within the $(MSA)_1 \cdot (MA)_1 \cdot (SFA^-)_1$ cluster increased, and the loop of complex was expanded. It has been demonstrated that SFA^- has the greatest capacity to stabilize MSA-MA clusters and facilitate MSA-MA nucleation in these clusters. This was attributed to its acidic nature and structural characteristics, which include a greater number of intermolecular hydrogen bond binding sites. Therefore, relative to the $(MSA)_1 \cdot (MA)_1 \cdot (X)_1$ cluster (Table 2), the Gibbs formation free energy ΔG of the $(MSA)_1 \cdot (MA)_1 \cdot (SFA^-)_1$ cluster was lower, indicating that the $NH_2SO_3^-$ ion exhibits a more potent nucleation capacity at the air–water interface compared to the X species in the gas phase. Consequently, our forecast was that the presence of $NH_2SO_3^-$ at the air–water interface would foster enhanced particle growth.

4 Summary and conclusions

In this study, quantum chemical calculations, BOMD simulations, and the ACDC kinetic model were utilized to characterize the gaseous and interfacial hydrolysis of $HNSO_2$ with MSA and to examine the influence exerted by SFA on MSA-MA-based clusters.

In the gaseous reaction, the activation energy for the hydrolysis of $HNSO_2$ catalyzed by MSA was only 0.8 kcal mol^{-1}, significantly lower by 7.7 kcal mol^{-1} than the energy barrier of H_2O-assisted $HNSO_2$ hydrolysis. The effective rate coefficients reveal that the SFA formation from MSA-catalyzed hydrolysis of $HNSO_2$ can be competitive with that catalyzed by H_2O within an altitude of 5–15 km. Moreover, kinetic simulations utilizing the ACDC have disclosed that SFA has an unexpectedly positive impact on the NPF process, markedly enhancing the assembly of the MSA-MA-based cluster. Notably, the "participant" mechanism of SFA for cluster formation was identified by tracing the growth paths of the system in agriculture-developed and coastal industrial areas, especially significant in the Yangtze River Delta of China, in Bangladesh, and on the east coast of India.

At the air–water interface, the $NH_2SO_3^-$ and H_3O^+ ion formation mechanism ($\sim 40\,\%$) and the proton exchange mechanism ($\sim 60\,\%$) were observed in the hydrolysis of $HNSO_2$ with MSA, which can take place in a few picoseconds. Notably, the SFA^-, MSA^-, and H_3O^+ ions formed at the air–water interface possess the ability to attract potential precursor molecules like MSA, MA, and HNO_3. This attraction facilitates the transition of gaseous molecules onto the surface of the water microdroplet. Moreover, the assessment of the potential of X in the formation of the ternary MSA-MA-X cluster revealed that SFA^- exhibits the greatest propensity

Table 2. Gibbs free energy (ΔG) for the formation of SFA^- … MSA, SFA^- … NA, SFA^- … OA, H_3O^+ … MA, MSA^- … MSA, MSA^- … OA, MSA^- … NA, and MSA … MA.$(MSA)_1 \cdot (MA)_1 \cdot (X)_1$ at 298 K.

	SFA^- … MSA	SFA^- … HNO_3	SFA^- … OA	MSA^- … MSA	MSA^- … NA
ΔG	−23.8	−21.5	−25.2	−23.9	−22.6
	MSA^- … OA	MSA … H_3O^+	MA … H_3O^+	MSA … MA	
ΔG	−25.8	−35.8	−57.9	−7.0 (−7.2)[b]	
	HCOOH … MSA … MA	CH_3COOH … MSA … MA	CHOCOOH … MSA … MA	OA … MSA … MA	
ΔG	−14.7 (−15.8)[a]	−14.8 (−14.3)[a]	−14.7 (−15.6)[a]	−13.3 (−12.7)[a]	
	$CH_3COCOOH$ … MSA … MA	$HOOCCH_2COOH$ … MSA … MA	$HOOC(CH)_2COOH$ … MSA … MA	$HOOC(CH_2)_2COOH$ … MSA … MA	
ΔG	−13.3 (−13.0)[a]	−14.7 (−16.7)[a]	−15.9 (−15.3)[a]	−13.9 (−14.3)[a]	
	$HOOC(CH_2)_3COOH$ … MSA … MA	$C_6H_5(COOH)$ … MSA … MA	$C_{10}H_{16}O_3$ … MSA … MA	SFA^- … MSA … MA	
ΔG	−18.9 (−17.9)[a]	−15.4 (−15.3)[a]	−16.4 (−15.3)[a]	−25.8	

[a] The value was taken from Zhang et al. (2022a). [b] The value was taken from Zhong et al. (2019).

to stabilize MSA-MA clusters and to foster the nucleation of MSA-MA in the context of X.

Overall, this work not only elucidates a novel mechanism underlying the hydrolysis of $HNSO_2$ with MSA but also highlights the potential contribution of SFA on aerosol particle growth and new particle formation.

Data availability. All data presented in this study are available upon request from the corresponding author.

Supplement. The supplement related to this article is available online at https://doi.org/10.5194/acp-25-2829-2025-supplement.

Author contributions. HW: methodology, validation, investigation, and writing (original draft). SW: writing (review), conceptualization, methodology, and investigation. JY: writing (review) and data computation. YY: data curation and data computation. RL: writing (editing), data curation, visualization, and investigation. RW: data curation, formal analysis, and funding acquisition. CZ: data curation, project administration, and writing (review and editing). TZ: methodology, formal analysis, and funding acquisition. CZ: writing (review and editing) and formal analysis.

Competing interests. The contact author has declared that none of the authors has any competing interests.

Disclaimer. Publisher's note: Copernicus Publications remains neutral with regard to jurisdictional claims made in the text, published maps, institutional affiliations, or any other geographical representation in this paper. While Copernicus Publications makes every effort to include appropriate place names, the final responsibility lies with the authors.

Acknowledgements. This work was supported by the National Natural Science Foundation of China (grant nos. 22073059 and 22203052).

Financial support. This research has been supported by the National Natural Science Foundation of China (grant nos. 22203052 and 22073059).

Review statement. This paper was edited by Fangqun Yu and reviewed by three anonymous referees.

References

Adler, T. B., Knizia, G., and Werner, H. J.: A simple and efficient CCSD(T)-F12 approximation, J. Chem. Phys., 127, 22 , https://doi.org/10.1021/jp910415a, 2007.

Anglada, J. M., Hoffman, G. J., Slipchenko, L. V. M., Costa, M., Ruiz-Lopez, M. F., and Francisco, J. S.: Atmospheric significance of water clusters and ozone-water complexes, J. Phys. Chem. A, 117, 10381–10396, 2013.

Bao, J. L., Zhang, X., and Truhlar, D. G.: Barrierless association of CF_2 and dissociation of C_2F_4 by variational transition-state theory and system-specific quantum Rice-Ramsperger-Kassel theory, P. Natl. Acad. Sci. USA., 113, 13606–13611, 2016.

Becke, A. D.: Density-functional exchange-energy approximation with correct asymptotic behavior, Phys. Rev. A., 38, 3098–3100, 1988.

Berresheim, H., Elste, T., Tremmel, H. G., Allen, A. G., Hansson, H. C., Rosman, K., Dal Maso, M., Mäkelä, J. M., Kulmala, M., and O'Dowd, C. D.: Gas-aerosol relationships of H_2SO_4, MSA, and OH: Observations in the coastal marine boundary layer at Mace Head, Ireland, J. Geophys. Res.-Atmos., 107, PAR 5-1–PAR 5-12, 2002.

Bork, N., Elm, J., Olenius, T., and Vehkamäki, H.: Methane sulfonic acid-enhanced formation of molecular clusters of sulfuric acid and dimethyl amine, Atmos. Chem. Phys., 14, 12023–12030, https://doi.org/10.5194/acp-14-12023-2014, 2014a.

Bork, N., Du, L., Reiman, H., Kurten, T., and Kjaergaard, H. G.: Benchmarking ab initio binding energies of hydrogen-bonded molecular clusters based on FTIR spectroscopy, J. Phys. Chem. A, 118, 5316–5322, 2014b.

Buszek, R. J., Torrent-Sucarrat, M., Anglada, J. M., and Francisco, J. S.: Effects of a single water molecule on the $OH + H_2O_2$ reaction, J. Phys. Chem. A, 116, 5821–5829, 2012.

Chen, D., Li, D., Wang, C., Luo, Y., Liu, F., and Wang, W.: Atmospheric implications of hydration on the formation of methanesulfonic acid and methylamine clusters: A theoretical study, Chemosphere., 244, 125538–125547, 2020.

Chen, H. and Finlayson-Pitts, B. J.: New particle formation from methanesulfonic acid and amines/ammonia as a function of temperature, Environ. Sci. Technol., 51, 243–252, 2017.

Chen, H., Varner, M. E., Gerber, R. B., and Finlayson-Pitts, B. J.: Reactions of methanesulfonic acid with amines and ammonia as a source of new particles in air, J. Phys. Chem. B, 120, 1526–1536, 2016.

Cheng, Y., Ding, C., Wang, H., Zhang, T., Wang, R., Muthiah, B., Xu, H., Zhang, Q., and Jiang, M.: Significant influence of water molecules on the $SO_3 + HCl$ reaction in the gas phase and at the air-water interface, Phys. Chem. Chem. Phys., 25, 28885–28894, 2023.

Chuang, Y., Corchado, J., Fast, P., Villa, J., Coitino, E., Hu, W., Liu, Y., Lynch, G., Nguyen, K., and Jackels, C.: Polyrate-version 8.2, University of Minnesota, Minneapolis, https://comp.chem.umn.edu/polyrate/ (last access: 7 March 2025), 1999.

Dawson, M. L., Varner, M. E., Perraud, V., Ezell, M. J., Gerber, R. B., and Finlayson-Pitts, B. J.: Simplified mechanism for new particle formation from methanesulfonic acid, amines, and water via experiments and ab initio calculations, P. Natl. Acad. Sci. USA, 109, 18719–18724, 2012.

Deng, G., Wu, Z., Li, D., Linguerri, R., Francisco, J. S., and Zeng, X. Q.: Simplest N-Sulfonylamine $HNSO_2$, J. Am. Chem. Soc., 140, 11509–11512, 2016.

Ding, C., Cheng, Y., Wang, H., Yang, J., Li, Z., Lily, M., Wang, R., and Zhang, T.: Determination of the influence of water on the $SO_3 + CH_3OH$ reaction in the gas phase and at the air-water interface, Phys. Chem. Chem. Phys., 25, 15693–15701, 2023.

Elm, J., Bilde, M., and Mikkelsen, K. V.: Assessment of density functional theory in predicting structures and free energies of reaction of atmospheric prenucleation clusters, J. Chem. Theory Comput., 8, 2071–2077, 2012.

Freeling, F., Scheurer, M., Sandholzer, A., Armbruster, D., Nödler, K., Schulz, M., Ternes, T. A., and Wick, A.: Under the radar – Exceptionally high environmental concentrations of the high production volume chemical sulfamic acid in the urban water cycle, Water Res., 175, 115706, https://doi.org/10.1016/j.watres.2020.115706, 2020.

Frisch, M. J., Trucks, G. W., Schlegel, H. B., Scuseria, G. E., Robb, M. A., Cheeseman, J. R., Scalmani, G., Barone, V., Mennucci, B., Petersson, G. A., Nakatsuji, H., Caricato, M., Li, X., Hratchian, H. P., Izmaylov, A. F., Bloino, J., Zheng, G., Sonnenberg, J. L., Hada, M., Ehara, M., Toyota, K., Fukuda, R., Hasegawa, J., Ishida, M., Nakajima, T., Honda, Y., Kitao, O., Nakai, H., Vreven, T., Montgomery Jr., J. A., Peralta, J. E., Ogliaro, F., Bearpark, M., Heyd, J. J., Brothers, E., Kudin, K. N., Staroverov, V. N., Kobayashi, R., Normand, J., Raghavachari, K., Rendell, A., Burant, J. C., Iyengar, S. S., Tomasi, J., Cossi, M., Rega, N., Millam, J. M., Klene, M., Knox, J. E., Cross, J. B., Bakken, V., Adamo, C., Jaramillo, J., Gomperts, R., Stratmann, R. E., Yazyev, O., Austin, A. J., Cammi, R., Pomelli, C., Ochterski, J. W., Martin, R. L., Morokuma, K., Zakrzewski, V. G., Voth, G. A., Salvador, P., Dannenberg, J. J., Dapprich, S., Daniels, A. D., Farkas, Ö., Foresman, J. B., Ortiz, J. V., Cioslowski, J., and Fox, D. J: Gaussian09 Revision D.01, Gaussian Inc., Wallingford, CT, http://www.gaussian.com (last access: 1 November 2016), 2009.

Georgievskii, Y. and Klippenstein, S.: Variable reaction coordinate transition state theory: analytic results and application to the $C_2H_3 + H \rightarrow C_2H_4$ reaction, J. Chem. Phlys., 118, 5442–5455, 2003.

Glowacki, D. R., Liang, C.-H., Morley, C., Pilling, M. J., and Robertson, S. H.: MESMER: an open-source master equation solver for multi-energy well reactions, J. Phys. Chem. A, 116, 9545–9560, 2012.

Goedecker, S., Teter, M., and Hutter, J.: Separable dual-space Gaussian pseudopotentials, Phys. Rev. B., 54, 1703, https://doi.org/10.1103/PhysRevB.54.1703, 1996.

Gonzalez, J., Anglada, J. M., Buszek, R. J., and Francisco, J. S.: Impact of water on the OH + HOCl reaction, J. Am. Chem. Soc., 133, 3345–3353, 2011.

Grimme, S., Antony, J., Ehrlich, S., and Krieg, H.: A consistent and accurate ab initio parametrization of density functional dispersion correction (DFT-D) for the 94 elements H-Pu, J. Chem. Phys., 132, 154104, https://doi.org/10.1063/1.3382344, 2010.

Hartwigsen, C., Gœdecker, S., and Hutter, J.: Relativistic separable dual-space Gaussian pseudopotentials from H to Rn, Phys. Rev. B, 58, 3641–3662, 1998.

Hirota, K., Mäkelä, J., and Tokunaga, O.: Reactions of sulfur dioxide with ammonia: Dependence on oxygen and nitric oxide, Ind. Eng. Chem. Res., 35, 3362–3368, 1996.

Hu, Y., Chen, S., Ye, S., Wei, S., Chu, B., Wang, R., Li, H., and Zhang, T.: The role of trifluoroacetic acid in new particle formation from methanesulfonic acid-methylamine, Atmos. Environ., 311, 120001, https://doi.org/10.1016/j.atmosenv.2023.120001, 2023.

Hutter, J., Iannuzzi, M., Schiffmann, F., and VandeVondele, J.: Cp2k: atomistic simulations of condensed matter systems, WIRES Comput. Mol. Sci., 4, 15–25, 2014.

Jung, J., Hong, S.-B., Chen, M., Hur, J., Jiao, L., Lee, Y., Park, K., Hahm, D., Choi, J.-O., Yang, E. J., Park, J., Kim, T.-W., and Lee, S.: Characteristics of methanesulfonic acid, non-sea-salt sulfate and organic carbon aerosols over the Amundsen Sea, Antarctica, Atmos. Chem. Phys., 20, 5404–5424, https://doi.org/10.5194/acp-20-5405-2020, 2020.

Kendall, R. A., Dunning Jr., T. H., and Harrison, R. J.: Electron affinities of the first-row atoms revisited. Systematic basis sets and wave functions, J. Chem. Phys., 96, 6796–6806, 1992.

Kim, T. O., Ishida, T., Adachi, M., Okuyama, K., and Seinfeld, J. H.: Nanometer-sized particle formation from $NH_3/SO_2/H_2O$/air mixtures by ionizing irradiation, Aerosol Sci. Tech., 29, 111–125, 1998.

Kolb, C., Jayne, J., Worsnop, D., Molina, M., Meads, R., and Viggiano, A.: Gas phase reaction of sulfur trioxide with water vapor, J. Am. Chem. Soc., 116, 10314–10315, 1994.

Kulmala, M., Vehkamäki, H., Petäjä, T., Dal Maso, M., Lauri, A., Kerminen, V. M., Birmili, W., and McMurry, P. H.: Formation and growth rates of ultrafine atmospheric particles: a review of observations, J. Aerosol Sci., 35, 143–176, 2004.

Kumar, M., Li, H., Zhang, X., Zeng, X. C., and Francisco, J. S.: Nitric acid-amine chemistry in the gas phase and at the air-water interface, J. Am. Chem. Soc., 140, 6456–6466, 2018.

Kuttippurath, J., Singh, A., Dash, S., Mallick, N., Clerbaux, C., Van Damme, M., Clarisse, L., Coheur, P.-F., Raj, S., and Abbhishek, K.: Record high levels of atmospheric ammonia over India: Spatial and temporal analyses, Sci. Total Environ., 740, 139986, https://doi.org/10.1016/j.scitotenv.2020.139986, 2020.

Larson, L. J. and Tao, F.-M.: Interactions and reactions of sulfur trioxide, water, and ammonia: An ab initio and density functional theory study, J. Phys. Chem. A, 105, 4344–4350, 2001.

Lee, C., Yang, W., and Parr, R. G.: Development of the colle-Salvetti correlation-energy formula into a functional of the electron density, Phys. Rev. B, 37, 785, https://doi.org/10.1103/PhysRevB.37.785, 1988.

Li, H., Zhong, J., Vehkamäki, H., Kurtén, T., Wang, W., Ge, M., Zhang, S., Li, Z., Zhang, X., Francisco, J. S., and Zeng, X. C.: Self-Catalytic reaction of SO_3 and NH_3 to produce sulfamic acid and its implication to atmospheric particle formation, J. Am. Chem. Soc., 140, 11020–11028, 2018.

Liu, J., Liu, Y., Yang, J., Zeng, X. C., and He, X.: Directional proton transfer in the reaction of the simplest criegee intermediate with water involving the formation of transient H_3O^+, J. Phys. Chem. Lett., 12, 3379–3386, https://doi.org/10.1021/acs.jpclett.1c00448, 2021a.

Liu, L., Yu, F., Tu, K., Yang, Z., and Zhang, X.: Influence of atmospheric conditions on the role of trifluoroacetic acid in atmospheric sulfuric acid–dimethylamine nucleation, Atmos.

Chem. Phys., 21, 6221–6230, https://doi.org/10.5194/acp-21-6221-2021, 202b1.

Long, B., Chang, C.-R., Long, Z.-W., Wang, Y.-B., Tan, X.-F., and Zhang, W.-J.: Nitric acid catalyzed hydrolysis of SO_3 in the formation of sulfuric acid: a theoretical study, Chem. Phys. Lett., 581, 26–29, 2013.

Long, B., Wang, Y., Xia, Y., He, X., Bao, J. L., and Truhlar, D. G.: Atmospheric Kinetics: Bimolecular Reactions of Carbonyl Oxide by a Triple-Level Strategy, J. Am. Chem. Soc., 143, 8402–8413, 2021.

Long, B., Xia, Y., Zhang, Y.-Q., and Truhlar, D. G.: Kinetics of sulfur trioxide reaction with water vapor to form atmospheric sulfuric acid, J. Am. Chem. Soc., 145, 19866–19876, 2023.

Lovejoy, E. R. and Hanson, D. R.: Kinetics and products of the reaction $SO_3 + NH_3 + N_2$, J. Phys. Chem., 100, 4459–4465, 1996.

Ma, X., Zhao, X., Huang, Z., Wang, J., Lv, G., Xu, F., Zhang, Q., and Wang, W.: Determination of reactions between Criegee intermediates and methanesulfonic acid at the gas-liquid interface, Sci. Total Environ., 707, 135804, https://doi.org/10.1016/j.scitotenv.2019.135804, 2020.

Mai, T. V. T., Duong, M. V., Nguyen, H. T., and Huynh, L. K.: Ab initio kinetics of the $HOSO_2 + {}^3O_2 \rightarrow SO_3 + HO_2$ reaction, Phys. Chem. Chem. Phys., 20, 6677–6687, 2018.

Manonmani, G., Sandhiya, L., and Senthilkumar, K.: Hydrolysis of $HNSO_2$: A potential route for atmospheric production of H_2SO_4 and NH_3, Int. J. Quant. Chem., 120, e26182, https://doi.org/10.1002/qua.26182, 2020.

Mansour, K., Decesari, S., Bellacicco, M., Marullo, S., Santoleri, R., Bonasoni, P., Facchini, M. C., Ovadnevaite, J., Ceburnis, D., and O'Dowd, C.: Particulate methanesulfonic acid over the central Mediterranean Sea: source region identification and relationship with phytoplankton activity, Atmos. Res., 237, 104837, https://doi.org/10.1016/j.atmosres.2019.104837, 2020.

Mao, J., Yu, F., Zhang, Y., An, J., Wang, L., Zheng, J., Yao, L., Luo, G., Ma, W., Yu, Q., Huang, C., Li, L., and Chen, L.: High-resolution modeling of gaseous methylamines over a polluted region in China: source-dependent emissions and implications of spatial variations, Atmos. Chem. Phys., 18, 7933–7950, https://doi.org/10.5194/acp-18-7933-2018, 2018.

McGrath, M. J., Olenius, T., Ortega, I. K., Loukonen, V., Paasonen, P., Kurtén, T., Kulmala, M., and Vehkamäki, H.: Atmospheric Cluster Dynamics Code: a flexible method for solution of the birth-death equations, Atmos. Chem. Phys., 12, 2345–2355, https://doi.org/10.5194/acp-12-2345-2012, 2012.

Meana-Pañeda, R., Zheng, J., Bao, J. L., Zhang, S., Lynch, B. J., Corchado, J. C., Chuang, Y.-Y., Fast, P. L., Hu, W.-P., and Liu, Y.-P.: Polyrate 2023: A computer program for the calculation of chemical reaction rates for polyatomics. New version announcement, Comput. Phys. Commun., 294, 108933, https://doi.org/10.1016/j.cpc.2023.108933, 2024.

Neese, F.: The ORCA program system, WIREs Comput. Mol. Sci., 2, 73–78, 2012.

Nishino, N., Arquero, K. D., Dawson, M. L., and Finlayson-Pitts, B. J.: Infrared studies of the reaction of methanesulfonic acid with trimethylamine on surfaces, Environ. Sci. Technol., 48, 323–330, https://doi.org/10.1021/es403845b, 2014.

Parandaman, A., Perez, J. E., and Sinha, A.: Atmospheric decomposition of trifluoromethanol catalyzed by formic acid, J. Phys. Chem. A, 122, 9553–9562, 2018.

Pszona, M., Haupa, K., Bil, A., Mierzwicki, K., Szewczuk, Z., and Mielke, Z.: Clustering of sulfamic acid: ESI MS and theoretical study, J. Mass Spectrom., 50, 127–135, 2015.

Rennebaum, T., van Gerven, D., Sebastian, S. S., and Wickleder, M. S.: Hydrazine sulfonic acid, $NH_3NH(SO_3)$, the bigger sibling of sulfamic acid, Chem.-Eur. J., 30, e202302526, https://doi.org/10.1002/chem.202302526, 2024.

Saltzman, E., Savoie, D., Prospero, J., and Zika, R.: Methanesulfonic acid and non-sea-salt sulfate in Pacific air: Regional and seasonal variations, J. Atmos. Chem., 4, 227–240, 1986.

Sarkar, S., Mallick, S., Kumar, P., and Bandyopadhyay, B.: Isomerization of methoxy radical in the troposphere: Competition between acidic, neutral and basic catalysts, Phys. Chem. Chem. Phys., 19, 27848–27858, 2017.

Shen, J., Xie, H.-B., Elm, J., Ma, F., Chen, J., and Vehkamaki, H.: Methanesulfonic acid-driven new particle formation enhanced by monoethanolamine: A computational study, Environ. Sci. Technol., 53, 14387–14397, 2019.

Shen, J., Elm, J., Xie, H.-B., Chen, J., Niu, J., and Vehkamaki, H.: Structural effects of amines in enhancing methanesulfonic acid-driven new particle formation, Environ. Sci. Technol., 54, 13498–13508, 2020.

Shi, Z., Ford, J., and Castleman Jr., A.: Cluster reactions of surlfur trioxide and ammonia, Chem. Phys. Lett., 220, 274–280, 1994.

Tang, Y. S., Flechard, C. R., Dämmgen, U., Vidic, S., Djuricic, V., Mitosinkova, M., Uggerud, H. T., Sanz, M. J., Simmons, I., Dragosits, U., Nemitz, E., Twigg, M., van Dijk, N., Fauvel, Y., Sanz, F., Ferm, M., Perrino, C., Catrambone, M., Leaver, D., Braban, C. F., Cape, J. N., Heal, M. R., and Sutton, M. A.: Pan-European rural monitoring network shows dominance of NH_3 gas and NH_4NO_3 aerosol in inorganic atmospheric pollution load, Atmos. Chem. Phys., 21, 875–914, https://doi.org/10.5194/acp-21-875-2021, 2021.

Tsona Tchinda, N., Du, L., Liu, L., and Zhang, X.: Pyruvic acid, an efficient catalyst in SO_3 hydrolysis and effective clustering agent in sulfuric-acid-based new particle formation, Atmos. Chem. Phys., 22, 1951–1963, https://doi.org/10.5194/acp-22-1951-2022, 2022.

VandeVondele, J. and Hutter, J.: Gaussian basis sets for accurate calculations on molecular systems in gas and condensed phases, J. Chem. Phys., 127, 114105, https://doi.org/10.1063/1.2770708, 2007.

VandeVondele, J., Krack, M., Mohamed, F., Parrinello, M., Chassaing, T., and Hutter, J.: Quickstep: Fast and accurate density functional calculations using a mixed Gaussian and plane waves approach, Comput. Phys. Commun., 167, 103–128, 2005.

Van Stempvoort, D., Spoelstra, J., Brown, S., Robertson, W., Post, R., and Smyth, S.: Sulfamate in environmental waters, Sci. Total Environ., 695, 133734, https://doi.org/10.1016/j.scitotenv.2019.133734, 2019.

Wang, R., Cheng, Y., Chen, S., Li, R., Hu, Y., Guo, X., Zhang, T., Song, F., and Li, H.: Reaction of SO_3 with H_2SO_4 and its implications for aerosol particle formation in the gas phase and at the air–water interface, Atmos. Chem. Phys., 24, 4029–4046, https://doi.org/10.5194/acp-24-4029-2024, 2024.

Warner, J. X., Wei, Z., Strow, L. L., Dickerson, R. R., and Nowak, J. B.: The global tropospheric ammonia distribution as seen in the 13-year AIRS measurement record, Atmos. Chem. Phys., 16, 5467–5479, https://doi.org/10.5194/acp-16-5467-2016, 2016.

Xue, J., Shao, X., Li, J., Li, J., Trabelsi, T., Francisco, J. S., and Zeng, X.: Observation of the Water-$HNSO_2$ complex, J. Am. Chem. Soc., 146, 5455–5460, 2024.

Yu, X., Shen, L., Hou, X., Yuan, L., Pan, Y., An, J., and Yan, S.: High-resolution anthropogenic ammonia emission inventory for the Yangtze River Delta, China, Chemosphere, 251, 126342, https://doi.org/10.1038/srep15842, 2020.

Zhang, J. and Dolg, M.: AB Cluster: the artificial bee colony algorithm for cluster global optimization, Phys. Chem. Chem. Phys., 17, 24173–24181, 2015.

Zhang, R., Shen, J., Xie, H.-B., Chen, J., and Elm, J.: The role of organic acids in new particle formation from methanesulfonic acid and methylamine, Atmos. Chem. Phys., 22, 2639–2650, https://doi.org/10.5194/acp-22-2639-2022, 2022a.

Zhang, T., Wen, M., Cao, X., Zhang, Y., Zeng, Z., Guo, X., Zhao, C., Lily, M., and Wang, R.: The hydrolysis of NO_2 dimer in small clusters of sulfuric acid: A potential source of nitrous acid in troposphere, Atmos. Environ., 243, 117876, https://doi.org/10.1016/j.atmosenv.2020.117876, 2020.

Zhang, T., Wen, M., Ding, C., Zhang, Y., Ma, X., Wang, Z., Lily, M., Liu, J., and Wang, R.: Multiple evaluations of atmospheric behavior between Criegee intermediates and HCHO: Gas-phase and gas-liquid interface reaction, J. Environ. Sci., 127, 308–319, 2023a.

Zhang, T., Wen, M., Zhang, Y., Lan, X., Long, B., Wang, R., Yu, X., Zhao, C., and Wang, W.: Atmospheric chemistry of the self-reaction of HO_2 radicals: stepwise mechanism versus one-step process in the presence of $(H_2O)_n$ $(n = 1–3)$ clusters, Phys. Chem. Chem. Phys., 21, 24042–24053, 2019.

Zhang, T., Zhang, Y., Tian, S., Zhou, M., Liu, D., Lin, L., Zhang, Q., Wang, R., and Muthiah, B.: Possible atmospheric source of NH_2SO_3H: the hydrolysis of $HNSO_2$ in the presence of neutral, basic, and acidic catalysts, Phys. Chem. Chem. Phys., 24, 4966–4977, 2022b.

Zhang, X., Lian, Y., Tan, S., and Yin, S.: Organosulfate produced from consumption of SO_3 speeds up sulfuric acid–dimethylamine atmospheric nucleation, Atmos. Chem. Phys., 24, 3593–3612, https://doi.org/10.5194/acp-24-3593-2024, 2024.

Zhang, Y., Wang, Z., Wang, H., Cheng, Y., Zhang, T., Ou, T., and Wang, R.: Atmospheric chemistry of NH_2SO_3H in polluted areas: an unexpected isomerization of NH_2SO_3H in acid-polluted regions, J. Phys. Chem. A, 127, 8935–8942, 2023b.

Zhao, X., Shi, X., Ma, X., Zuo, C., Wang, H., Xu, F., Sun, Y., and Zhang, Q.: 2-Methyltetrol sulfate ester-initiated nucleation mechanism enhanced by common nucleation precursors: A theory study, Sci. Total Environ., 723, 137987, https://doi.org/10.1016/j.scitotenv.2020.137987, 2020.

Zhao, Y. and Truhlar, D. G.: The M06 suite of density functionals for main group thermochemistry, thermochemical kinetics, noncovalent interactions, excited states, and transition elements: two new functionals and systematic testing of four M06-class functionals and 12 other functionals, Theor. Chem. Acc., 120, 215–241, 2008.

Zhong, J., Kumar, M., Zhu, C. Q., Francisco, J. S., and Zeng, X. C.: Frontispiece: surprising stability of larger criegee intermediates on aqueous interfaces, Angew. Chem. Int. Edit., 56, 7740–7744, 2017.

Zhong, J., Kumar, M., Francisco, J. S., and Zeng, X. C.: Insight into chemistry on cloud/aerosol water surfaces, Acc. Chem. Res., 51, 1229–1237, 2018.

Zhong, J., Li, H., Kumar, M., Liu, J., Liu, L., Zhang, X., Zeng, X. C., and Francisco, J. S.: Mechanistic insight into the reaction of organic acids with SO_3 at the air-water interface, Angew. Chem. Int. Edit., 131, 8351–8355, 2019.

Zhu, C., Kumar, M., Zhong, J., Li, L., Francisco, J. S., and Zeng, X. C.: New mechanistic pathways for Criegee-water chemistry at the air/water interface, J. Am. Chem. Soc., 138, 11164–11169, 2016.